Nano Research

Open Access

Research Article

Structural regulation of chitosan-assisted self-assembled MXene@1T-MoS_2 composite aerogels for high-efficiency absorption electromagnetic shielding performance

Shujiang Sun[§], Shijie Liu[§], Zhanyu Shen, Zhe Feng, Wenkun Fei, Xu He, Wanping Zhang ✉, Bo Li ✉, and Longlu Wang ✉

College of Electronic and Optical Engineering & College of Flexible Electronics (Future Technology), Nanjing University of Posts & Telecommunications, Nanjing 210023, China

[§] *Shujiang Sun and Shijie Liu contributed equally to this work.*

Cite this article: *Nano Research*, **2026**, *19*, 94908766. https://doi.org/10.26599/NR.2026.94908766

ABSTRACT: Rapid development of the fifth-generation wireless communication technology (5G) has made electromagnetic interference (EMI) a critical threat to electronic operations and human health. To mitigate severe secondary scattering caused by impedance mismatch in traditional materials, this study proposes a chitosan-assisted self-assembly strategy for two-dimensional (2D) materials. Using directional freezing and freeze-drying, MXene@1T-MoS_2/chitosan composite aerogels with a lamellar porous structure were successfully fabricated. The regulatory effects of chitosan viscosity on microscopic morphology, conductive network construction, and shielding performance were systematically investigated. Results show that medium-viscosity chitosan induces an optimal layered skeleton, enabling sufficient multiple reflection losses within the aerogel. To further enhance absorption-dominated shielding, metallic 1T-MoS_2 was introduced to construct heterointerfaces. Characterization and electromagnetic analysis confirm that the synergy between 1T-MoS_2, MXene, and the chitosan matrix significantly enhances interfacial and dipole polarization losses. Experimental results indicate that the composite aerogels exhibit excellent EMI shielding performance in the X-band, with the absorption coefficient increasing by 0.14 after the introduction of 1T-MoS_2. Furthermore, far-field simulations reveal that the optimized aerogels achieve a remarkable radar cross-section (RCS) reduction, consistently maintaining scattered signal intensities below −20 dB·m^2 across a wide angular range. Mechanism analysis reveals that the high shielding efficiency stems from the organic synergy of conductive loss, multi-component-induced polarization loss, and multiple reflection effects triggered by the lamellar porous structure. This study successfully achieves a fundamental shift in the shielding mechanism from interfacial reflection to high-efficiency absorption, providing a new experimental basis and design strategy for developing lightweight, high-absorption EMI shielding materials.

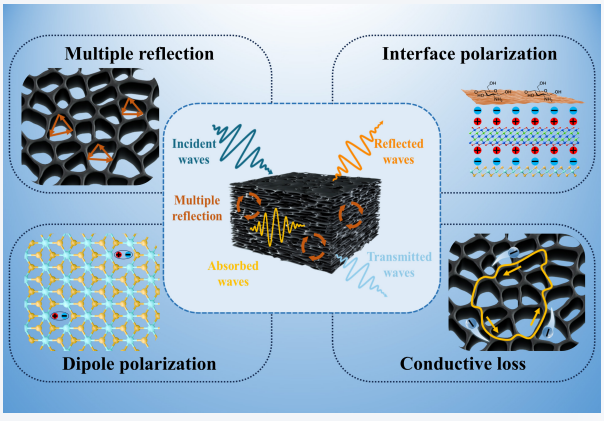

KEYWORDS: electromagnetic interference shielding, MXene, 1T-MoS_2, heterogeneous structure, lyophilization, low reflection

1 Introduction

With the rapid proliferation of 5G technology, the large-scale application of various electronic devices in daily life has led to significant electromagnetic (EM) pollution [1, 2]. This EM pollution not only interferes with the normal operation of high-sensitivity electronic equipment but also poses potential threats to human health [3, 4]. Currently, electromagnetic interference (EMI) shielding technology is regarded as the most effective solution to counteract EM pollution [5]. This technology utilizes specialized materials capable of reflecting and absorbing electromagnetic waves to effectively suppress or block the propagation of electromagnetic energy [6, 7]. Consequently, the development of advanced materials

Received: March 18, 2026; **Revised:** April 9, 2026
Accepted: April 20, 2026

✉Address correspondence to Wanping Zhang, vapine@njupt.edu.cn; Bo Li, elibo@njupt.edu.cn; Longlu Wang, wanglonglu@njupt.edu.cn

with superior EMI shielding performance has become a top priority in current electromagnetic protection research.

Traditional EMI shielding materials primarily rely on the reflection of EM waves to achieve their shielding functions [8]. Materials that utilize high electrical conductivity to achieve efficient shielding often suffer from severe impedance mismatch, which triggers intense electromagnetic reflection and subsequently exacerbates secondary scattering pollution [9, 10]. To mitigate this issue, it is essential to develop absorption-dominated EMI shielding materials. Such materials can effectively absorb the majority of incident EM waves, thereby reducing penetration and secondary scattering while achieving significant attenuation of EM radiation. Porous structures can regulate the equivalent wave impedance of a material [11], making it closer to that of free space. This not only reduces reflection at the material surface but also induces more EM waves to enter the material interior. Once inside, the hierarchical pore structures trigger multiple reflections and scattering, effectively prolonging the energy dissipation path [12]. Regarding material selection, in addition to traditional metals, certain high-conductivity non-metallic nanomaterials, such as transition metal carbides (MXenes) and transition metal dichalcogenides (TMDs), are increasingly becoming the focus of research for high-efficiency absorption-type shielding due to their unique two-dimensional (2D) structures and tunable surface chemistry.

MXenes represent an emerging class of 2D nanomaterials characterized by abundant surface functional groups, excellent electrical conductivity, and good flexibility [13–15]. Unlike graphene, which often suffers from degraded conductivity following oxidation or modification, MXenes overcome this limitation and have thus garnered widespread attention. $Ti_3C_2T_x$ is a quintessential MXene material that has attracted significant interest in the EMI shielding field due to its outstanding conductivity, mechanical properties, and chemical stability [16]. However, the high conductivity of $Ti_3C_2T_x$ nanosheets often causes the material's characteristic impedance to deviate severely from that of free space, leading to strong impedance mismatch at the surface. This high reflectivity not only prevents EM waves from entering the material interior for dissipation but also causes serious secondary EM radiation pollution [17]. To reduce this pollution, it is necessary to minimize surface reflection to allow more EM waves to penetrate the material [18]. Therefore, in-depth research into the structure and EMI shielding mechanisms of MXene-based composites is of great significance for the design and development of novel shielding materials that combine high absorption rates with low reflectivity. In 2018, S. Zhao et al. [19] successfully constructed highly conductive and ordered porous MXene/RGO composite aerogels using graphene oxide-assisted assembly and directional freezing techniques. They achieved efficient EMI shielding performance in epoxy composites at extremely low MXene loadings, providing crucial insights for the three-dimensional (3D) macroscopic assembly of MXenes and their application in functional composite materials.

Although the impedance matching of MXene-based materials can be partially improved through 3D porous structural design, the loss mechanism of a single-component system remains relatively simple, often making it difficult to achieve high-level absorption attenuation. Research indicates that constructing heterostructures based on 2D materials is an effective strategy for modulating the complex permittivity, optimizing impedance matching, and introducing additional loss mechanisms [20, 21]. Among various candidate materials, TMDs have become ideal choices for constructing high-performance composite shielding materials due to their tunable electronic states and layered characteristics highly compatible with MXenes. As a prominent TMD, MoS_2 possesses a graphite-like layered structure, which grants it immense potential in functional material applications [22]. In its typical layered configuration, a molybdenum atom layer is bonded to two sulfur atom layers via Van der Waals forces, forming a stable sandwich interlayer structure [23]. In addition to the common semiconducting phases (2H and 3R phases), MoS_2 also exhibits an important metallic polymorph known as the 1T phase [24]. Its electrical conductivity originates from the octahedral coordination structure between molybdenum and sulfur atoms, which allows excited electrons under an alternating electromagnetic field to move more freely within the lattice, thereby generating a robust response to EMI. However, reports regarding 1T-MoS_2 and MXene composites in the field of EMI shielding remain scarce.

Based on the aforementioned research background and addressing the key challenges in structural regulation, interfacial compatibility, and performance optimization of MXene materials for EMI shielding applications, this study proposes a novel 2D material self-assembly strategy assisted by chitosan. As a natural cationic polysaccharide, chitosan possesses excellent biocompatibility and abundant amino functional groups. It serves as an effective interfacial regulator and structure-directing agent, enabling controllable self-assembly with negatively charged MXene nanosheets through electrostatic interactions. On this basis, by further combining directional freezing techniques with vacuum freeze-drying processes, we successfully constructed MXene/chitosan composite aerogels with a highly ordered lamellar porous structure. This architecture exhibits excellent EMI shielding performance in the X-band, with an electromagnetic wave absorption rate exceeding 50%. To further enhance the EM wave absorption capacity, 1T-MoS_2 with high dielectric loss characteristics was introduced into the MXene/chitosan system. The experimental data reveal that the introduction of 1T-MoS_2 substantially augments the absorption capacity of the aerogels. An increase of about 0.14 in the absorption coefficient was achieved without compromising the outstanding overall EMI shielding effectiveness. Comparative analysis reveals that the introduction of 1T-MoS_2 effectively enhances polarization relaxation and interfacial loss mechanisms, thereby significantly promoting EM wave absorption. This finding not only proves the efficacy of multi-component synergy in improving shielding performance but also provides new insights and experimental evidence for designing a new generation of EMI shielding materials that combine high-efficiency absorption with lightweight characteristics.

2 Experimental section

2.1 Materials

Hydrofluoric acid (HF) and 99% acetic acid were purchased from Nanjing Chemical Reagent Co., Ltd. (Nanjing, China). Ti_3AlC_2 powder was obtained from Jiangsu Xianfeng Nanomaterials Technology Co., Ltd. (Nanjing, China). Commercial MoS_2 powder was acquired from Songhu Shenjian Technology Co., Ltd.

(Dongguan, China). n-Butyllithium (C_4H_9Li) and chitosan powder were supplied by Macklin Biochemical Co., Ltd. (Shanghai, China).

2.2 Characterization and measurement

X-ray photoelectron spectroscopy (XPS) analysis was performed on a Thermo Scientific K-Alpha instrument (USA). The morphologies of the samples were observed using a scanning electron microscope (SEM, TESCAN MIRA LMS, Czech Republic) and a transmission electron microscope (TEM, FEI Talos F200X, Czech Republic).

The electrical conductivity of the samples was measured using a four-probe tester (ST2263, Suzhou Jingge Electronics Co., Ltd., China). The EMI shielding performance in the X-band was measured using a vector network analyzer (VNA, ZVA24, Rohde & Schwarz, Germany) equipped with a WR-90 rectangular waveguide. The aerogel specimens were precisely tailored into dimensions of 22.86 mm × 10.16 mm × 3 mm to ensure a perfect fit within the rectangular waveguide. Relevant electromagnetic parameters, including the total shielding effectiveness (SE_T), reflection coefficient (R), and absorption coefficient (A) [25], were calculated from the measured scattering parameters (S-parameters) according to the following equations

$$R = |S_{11}|^2 \tag{1}$$

$$A = 1 - |S_{11}|^2 - |S_{21}|^2 \tag{2}$$

$$SE_R = -10\lg\left(1 - |S_{11}|^2\right) \tag{3}$$

$$SE_A = -10\lg\left[|S_{21}|^2 / \left(1 - |S_{11}|^2\right)\right] \tag{4}$$

$$EMI\ SE = SE_R + SE_A \tag{5}$$

The complex permittivity is calculated using the Nicolson–Ross–Weir (NRW) algorithm [26]. In the NRW algorithm, the reflection coefficient γ is given by the following equations

$$\Gamma = K \pm \sqrt{K^2 - 1} \tag{6}$$

with

$$K = \left(S_{11}^2 - S_{21}^2 + 1\right) / 2S_{11} \tag{7}$$

The positive or negative sign in Eq. (6) is determined by requiring $|\gamma| \leq 1$. The transmission coefficient T is given by

$$T = \left(S_{11} + S_{21} - \Gamma\right) / \left[1 - \left(S_{11} + S_{21}\right)\Gamma\right] \tag{8}$$

Accordingly, the permeability and permittivity are calculated from

$$\mu_r = (1+\Gamma) \Big/ \left[(1-\Gamma)\Lambda\sqrt{\left(1/\lambda_0^2\right) - \left(1/\lambda_c^2\right)}\right] \tag{9}$$

$$\varepsilon_r = \varepsilon' + j\varepsilon'' = \left[\left(1/\lambda_c^2\right) + \left(1/\Lambda^2\right)\right]\lambda_0^2/\mu_r \tag{10}$$

with

$$1/\Lambda^2 = -\left[\ln\left(1/T\right)/2\pi D\right]^2 \tag{11}$$

where λ_0 is the free-space wavelength; λ_c is the cutoff wavelength of the transmission line section; D is the thickness of the aerogel specimens.

2.3 Synthesis of $Ti_3C_2T_x$ MXene dispersion

$Ti_3C_2T_x$ was prepared through the selective etching of Ti_3AlC_2 using HF [27]. Briefly, 1 g of Ti_3AlC_2 powder was incrementally introduced into 50 mL of 40% HF solution under stirring for 24 h at ambient temperature. The selective removal of Al layers yielded accordion-like multi-layered $Ti_3C_2T_x$. Upon completion of the reaction, the obtained precipitate was dispersed in deionized water and sonicated in an ice bath for 10 min, followed by centrifugation at 4500 rpm for 5 min. After repeated washing cycles until the pH reached 6, a stable dispersion of monolayer or few-layer $Ti_3C_2T_x$ nanosheets was successfully obtained.

The supernatant was collected, and its concentration was adjusted via dilution. To prevent oxidative degradation and maintain structural stability, the delaminated MXene suspension was stored in a sealed container and briefly sonicated before each use to ensure uniform dispersibility.

2.4 Synthesis of 1T-MoS_2

High-purity 1T-MoS_2 was synthesized via a chemical lithium intercalation method [28]. Briefly, 0.6 g of bulk 2H-MoS_2 powder was dispersed in hexane under strictly anhydrous and anaerobic conditions within an inert atmosphere. Subsequently, 30 mL of n-butyllithium (C_4H_9Li) solution (1.6 M in hexane) was slowly introduced. The mixture was maintained at 80 °C for 36 h to facilitate the selective intercalation of lithium ions (Li^+) into the MoS_2 interlayers. This process triggered significant electron transfer and structural reconstruction, forming the intercalation compound $LiMoS_2$ and achieving the phase transition from the semiconducting 2H phase to the metallic 1T phase.

Upon completion of the reaction, the resulting product was thoroughly washed with hexane and vacuum-dried to obtain the pre-intercalated $LiMoS_2$. The $LiMoS_2$ powder was then uniformly dispersed in deionized (DI) water and subjected to intense ultrasonication in an ice bath for 60 min to induce exfoliation. During this stage, the dissolution of interlayer Li^+ caused the layered MoS_2 to dissociate into ultrathin nanosheets. Finally, the suspension was centrifuged at 20,000 rpm for 10 min to remove unexfoliated bulk materials and impurities. High-purity 1T-MoS_2 nanosheets were ultimately obtained after freeze-drying.

2.5 Fabrication of chitosan-assisted self-assembled MXene@1T-MoS_2 composite aerogels

First, a series of chitosan solutions (20 mg·mL^{-1}) with different viscosity levels were prepared by dissolving chitosan powders with varying degrees of deacetylation in a 1% (v/v) acetic acid solution under continuous stirring. The viscosity ranges were categorized as low (100–200 mPa·s), medium (200–400 mPa·s), and high (> 400 mPa·s). Subsequently, the MXene dispersion was mixed with the respective chitosan solutions in a 1:1 volume ratio. Following thorough stirring to ensure a homogeneous mixture, the resulting blend underwent ultrasonication to eliminate air bubbles. This degassing step was critical to prevent structural collapse or deformation of the aerogels caused by the pressure differential during the subsequent vacuum freeze-drying process. Ultimately, 3D hydrogels were constructed via electrostatic self-assembly between the negatively charged MXene nanosheets and the cationic chitosan chains.

To regulate the internal architecture, a directional freezing technique was employed [29]. The hydrogel was injected into an

epoxy resin mold fixed atop a high-thermal-conductivity iron block. The iron block was cooled by liquid nitrogen to establish a stable temperature gradient along the vertical axis through unidirectional heat conduction. This process drove the directional growth of ice crystals along the temperature gradient, achieving ordered solidification of the hydrogel.

The frozen samples were subsequently lyophilized to yield lightweight aerogels with a controlled thickness of 3 mm and a highly interconnected porous architecture. The obtained aerogels were named according to their composition: those prepared with medium-viscosity chitosan and MXene dispersions of 5, 10, and 20 mg·mL^{-1} were denoted as MCM-5, MCM-10, and MCM-20, respectively. Samples utilizing 10 mg·mL^{-1} MXene with low- and high-viscosity chitosan were labeled as LCM-10 and HCM-10.

To investigate the modulating effect of 1T-MoS_2 on electromagnetic wave absorption, 1T-MoS_2 powder was incorporated into the 10 mg·mL^{-1} MXene dispersion at a solid mass ratio of 5:1 (MXene to 1T-MoS_2) while maintaining the original preparation process of the MCM-10 aerogel unchanged. Through co-assembly and directional freezing, the MXene@1T-MoS_2/chitosan aerogel was successfully constructed and designated as MCMM-10.

3 Results and discussion

3.1 EM attenuation mechanism of composite aerogels

Single MXene (e.g., $Ti_3C_2T_x$) exhibits considerable potential for EMI shielding owing to its metal-like conductivity and abundant surface functional groups [30, 31]. However, in practical applications, the 2D nanosheets tend to restack densely. This restacking not only seriously deteriorates the impedance matching of the material, but also significantly compresses the multiple reflection paths of electromagnetic waves within it, ultimately leading to a shielding mechanism dominated by reflection and with limited effectiveness [32, 33]. Chitosan, a widely available natural polymer characterized by its biocompatibility and biodegradability, possesses abundant amino and hydroxyl groups along its molecular chains. These functional groups enable the construction of robust 3D crosslinked networks through hydrogen bonding and electrostatic interactions, rendering chitosan an ideal flexible scaffold for dispersing and anchoring 2D nanomaterials. Simultaneously, it imparts essential mechanical robustness and environmental stability to aerogel architectures [34–37]. Accordingly, by fabricating MXene and chitosan into an aerogel and constructing a 3D interconnected porous network, the stacking of layers can be effectively suppressed, and a significant structural multiple reflection effect can be introduced (Fig. 1(a)), causing electromagnetic waves to be repeatedly attenuated in the labyrinthine channels, thereby partially enhancing the absorption loss [38, 39]. Meanwhile, the high electrical conductivity of pure MXene results in a low interlayer contact resistance, which creates a significant disparity with the wave impedance of air, giving rise to severe impedance mismatch. Furthermore, a single reflection-dominated loss mechanism encounters a bottleneck when pursuing high absorption performance [40, 41]. In this context, the rational design of MXene@1T-MoS_2 composite aerogels emerges as a critical strategy to overcome these limitations. To further optimize the performance, metallic 1T-MoS_2 was introduced to create abundant heterointerfaces with the MXene nanosheets.

These heterointerfaces act as conductive bridges that optimize electron transport throughout the 3D network and induce pronounced interfacial polarization relaxation (Fig. 1(b)), thereby introducing a crucial dielectric loss pathway [42, 43]. In addition, the inherent dipolar polarization of 1T-MoS_2 (Fig. 1(c)) further improves the overall impedance-matching characteristics of the composite, enabling a larger fraction of incident electromagnetic waves to penetrate into the interior of the material [44, 45]. Simultaneously, the electromagnetic waves penetrating the interior of the material can induce eddy currents within the 3D conductive network (Fig. 1(d)) [46, 47]. The corresponding electromagnetic energy is directly converted into Joule heat and dissipated via this conductive loss mechanism. Serving as the structural backbone, chitosan firmly integrates all nanoscale constituents, endowing the aerogel with essential mechanical toughness and structural stability.

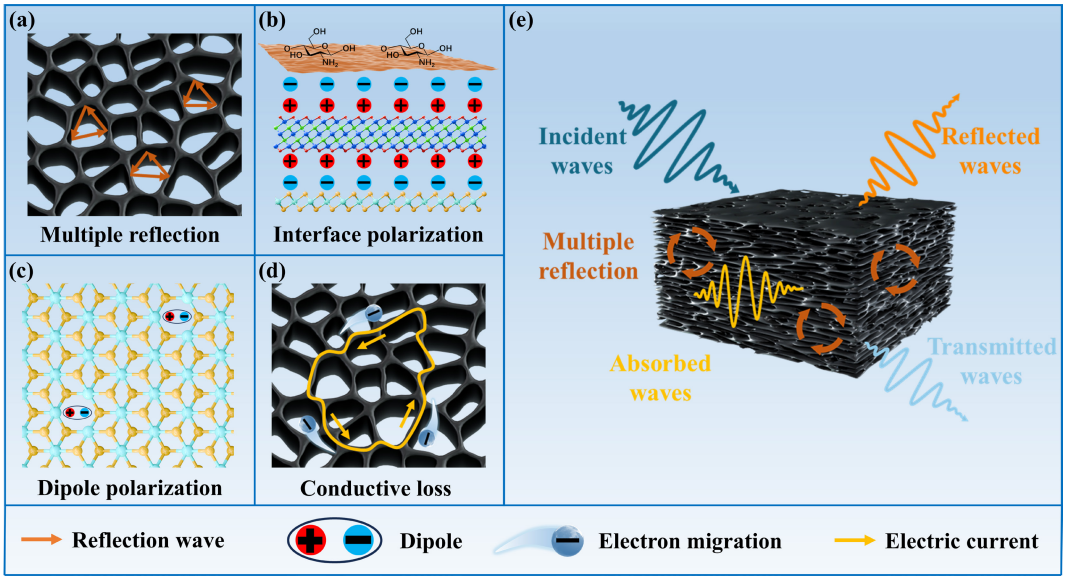

Figure 1 (a) Schematic illustration of electromagnetic wave attenuation via multiple internal reflections. (b) Schematic illustration of interfacial polarization among MXene, 1T-MoS_2, and chitosan components. (c) Schematic illustration of dipolar polarization in 1T-MoS_2. (d) Schematic illustration of the conductive loss mechanism. (e) Schematic illustration of the electromagnetic shielding mechanism of the MXene@1T-MoS_2 composite chitosan aerogel designed in this work.

As illustrated in Fig. 1(e), the core design concept of the MXene@1T-MoS_2 composite chitosan aerogel developed in this work lies in the synergistic integration of conductive loss, interfacial and dipole relaxation, and the multiple-internal-reflection attenuation effect induced by its multi-level porous structure. This synergy achieves a fundamental transformation of the electromagnetic shielding mechanism from interface reflection dominated to highly efficient absorption attenuation dominated.

3.2 Microscopic morphology analysis and structural characterization

$Ti_3C_2T_x$ nanosheets were synthesized via the HF etching method, as illustrated in Fig. 2(a). The precursor Ti_3AlC_2 was first treated with an HF solution to selectively dissolve the Al layers, resulting in accordion-like multilayer $Ti_3C_2T_x$ (m-$Ti_3C_2T_x$). Subsequently, monolayer or few-layer $Ti_3C_2T_x$ nanosheets were obtained by further ultrasonic exfoliation. High-purity 1T-MoS_2 nanosheets were synthesized using a chemical lithium intercalation method (Fig. 2(b)). Commercial MoS_2 powder was reacted with n-butyllithium under anhydrous and oxygen-free conditions, during which Li^+ ions were intercalated into the interlayers, inducing electron transfer and lattice distortion. Upon vigorous exfoliation in water, a dispersion of metallic 1T-MoS_2 was obtained. As shown in Fig. 2(c), the 1T-MoS_2 powder was uniformly mixed with an aqueous dispersion of $Ti_3C_2T_x$. This mixture was then added to a dilute acetic acid solution of chitosan under continuous stirring. Relying on the electrostatic interactions between the negatively charged nanosheets and the positively charged chitosan, a 3D hydrogel framework was rapidly established. Subsequently, after freeze-drying, a lightweight aerogel with a continuous porous structure was obtained by the ice-templating method (Fig. S1 in the Electronic supplementary material (ESM)).

For the MXene, the SEM image in Fig. 3(a) exhibits a typical fluffy and wrinkled morphology with interwoven and stacked nanosheets. This structure provides abundant interfaces and defect sites, forming a structural foundation for polarization loss and multiple reflections. The TEM image in Fig. 3(b) further confirms its ultrathin and flexible nanosheet characteristics. Such flexibility is conducive to forming a continuous coating on the aerogel scaffold and achieving effective interfacial bonding with other materials during subsequent compositing. The high-resolution TEM (HRTEM) image in Fig. 3(c) reveals a lattice spacing of 0.26 nm, indexed to the (100) crystal plane of MXene, with the lattice points confirming its hexagonal crystal structure. Furthermore, EDS elemental mapping (Fig. S3 in the ESM) shows a uniform distribution of Ti, C, O, and F elements across the nanosheets. The distinct Ti 2p and F 1s peaks in the XPS survey spectrum (Fig. S2(a) in the ESM) further verify the successful preparation of MXene. Regarding the 1T-MoS_2, the SEM image in Fig. 3(d) presents a stacked and interlaced layer structure, which can introduce a substantial number of interfaces and defects. The TEM image in Fig. 3(e) shows semi-transparent, wrinkled 2D nanosheets, whose curled edges demonstrate ultrathin flexibility, aiding in the construction of a 3D continuous conductive network within the composite system. In the HRTEM image (Fig. 3(f)), lattice fringes with a spacing of 0.29 nm are observed, indexed to the (002) crystal plane of 1T-MoS_2. The unique trigonal lattice arrangement and the XPS spectrum of Mo 3d (Fig. S2(b) in the ESM) confirm the presence of the metallic phase (1T phase). The TEM image and corresponding elemental mapping of 1T-MoS_2 are shown in Fig. S4 in the ESM. The XPS spectrum of the Mo element in 1T-MoS_2 is presented in Fig. S2(b) in the ESM. Figures 3(g)–3(i) reveals the decisive influence of chitosan viscosity on the microstructure of the aerogel matrix. The sample prepared from low-viscosity solution forms a dense, sheet-like stacked structure with almost no internal pores (Fig. 3(g)). The medium-viscosity sample exhibits the optimal porous lamellar structure, featuring uniformly distributed micropores between the macroscopic layered scaffolds (Fig. 3(h)). In contrast, the high-viscosity sample shows the formation of pores, but the lamellar structure is loose and exhibits poor connectivity (Fig. 3(i)).

3.3 EMI shielding performance and dielectric response

To investigate the influence of microscopic morphology and component characteristics on the EMI shielding performance of chitosan-based aerogels, this work focused on the synergistic mechanism between the microstructure of the aerogels and the concentration of the MXene dispersion as well as the loading of 1T-MoS_2 (which modulates electromagnetic loss properties). The EMI shielding effectiveness (SE) of the samples in the X-band was characterized using the waveguide method (Fig. S5 in the ESM). The results indicated that all aerogel samples exhibited excellent frequency independence across the tested band (Fig. 4(a)).

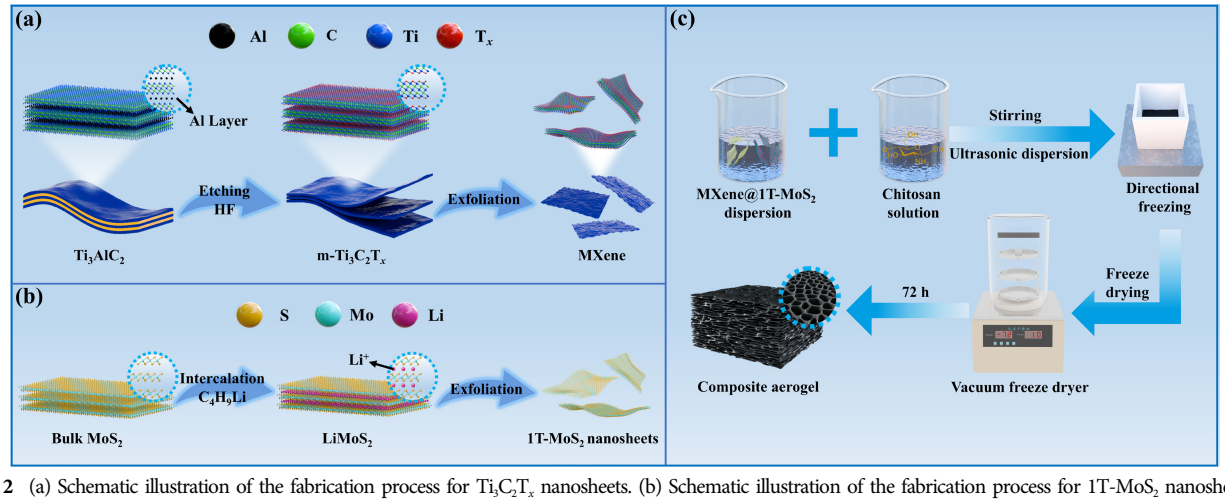

Figure 2 (a) Schematic illustration of the fabrication process for $Ti_3C_2T_x$ nanosheets. (b) Schematic illustration of the fabrication process for 1T-MoS_2 nanosheets. (c) Schematic illustration of the fabrication process for the 3D MXene@1T-MoS_2 composite aerogel.

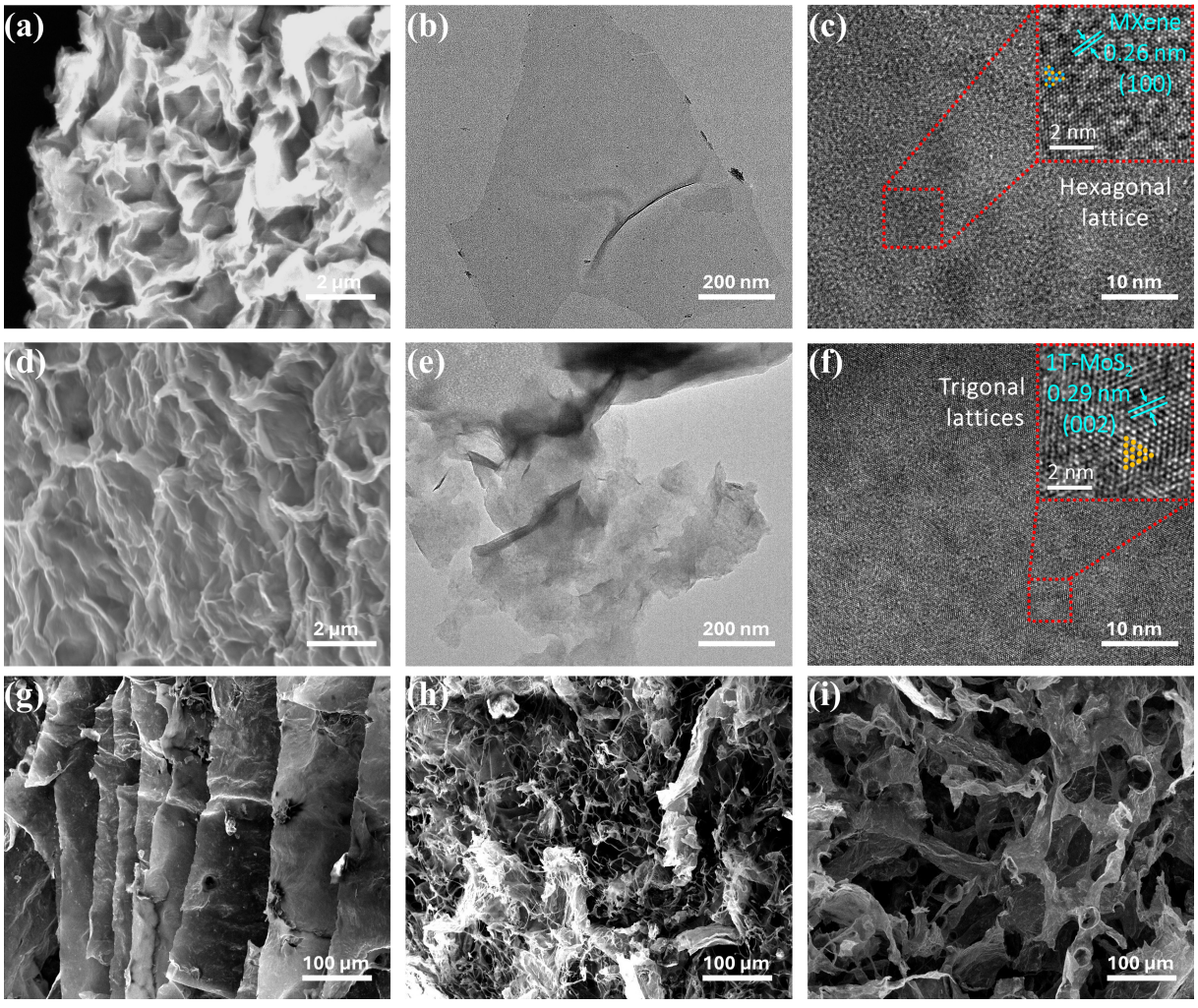

Figure 3 (a) SEM image, (b) TEM image, and (c) HRTEM image of Mxene. (d) SEM image, (e) TEM image, and (f) HRTEM image of 1T-MoS_2. (g)–(i) SEM images of chitosan aerogels with low, medium, and high viscosities, respectively.

As the MXene concentration increased, the electrical conductivity of the composite aerogels showed a stepwise enhancement. For instance, the conductivity of MCM-20 was approximately twice that of MCM-10, driving a significant upward trend in the SE_T. Notably, under identical filler loadings, aerogels constructed from medium-viscosity chitosan exhibited a unique porous lamellar stacked structure. This architecture integrates a substantial number of micropores within the layered scaffold, greatly facilitating the formation of a continuous and comprehensive 3D conductive network in the composite aerogel [48, 49]. As shown in Fig. 4(b), the medium-viscosity system (MCM-10) demonstrated significantly superior electrical conductivity compared to the structurally looser low-viscosity (LCM-10) and high-viscosity (HCM-10) systems, both of which exhibited conductivities below 2 $S \cdot m^{-1}$. Concurrently, this complex hierarchical porous structure can effectively induce multiple internal reflections of electromagnetic waves and significantly prolong their propagation path within the material. Under the synergistic effect of excellent conductivity and structure-induced effects, the EMI shielding performance of the medium-viscosity system was markedly superior to that of the low-viscosity or high-viscosity counterparts, demonstrating stronger electromagnetic wave dissipation capability.

Analysis of the power coefficients (Fig. 4(c)) further reveals the intrinsic mechanism of interaction between the aerogels and electromagnetic waves. The results indicate that the significant increase in material conductivity with higher MXene loading triggers severe impedance mismatch. During electromagnetic wave transmission, the excessively high carrier concentration causes the characteristic impedance at the material surface to be far lower than that of free space, thereby substantially enhancing reflection behavior at the interface. Particularly in the sample with the highest conductivity, MCM-20, its R value reached a maximum while its A value dropped to the lowest. This evolution confirms that although high conductivity is beneficial for improving total SE, excessive construction of the conductive network causes a large portion of the incident waves to be strongly reflected immediately upon contact with the material surface, limiting the ability of the wave energy to enter the material interior for attenuation [50–52]. Therefore, optimizing impedance matching and balancing the relationship between reflection and absorption is the key to achieving high-performance absorption-dominated shielding materials.

To suppress secondary scattering pollution from electromagnetic waves and pursue high absorption characteristics, MCM-10 was selected as the optimized matrix, and 1T-MoS_2 was introduced to

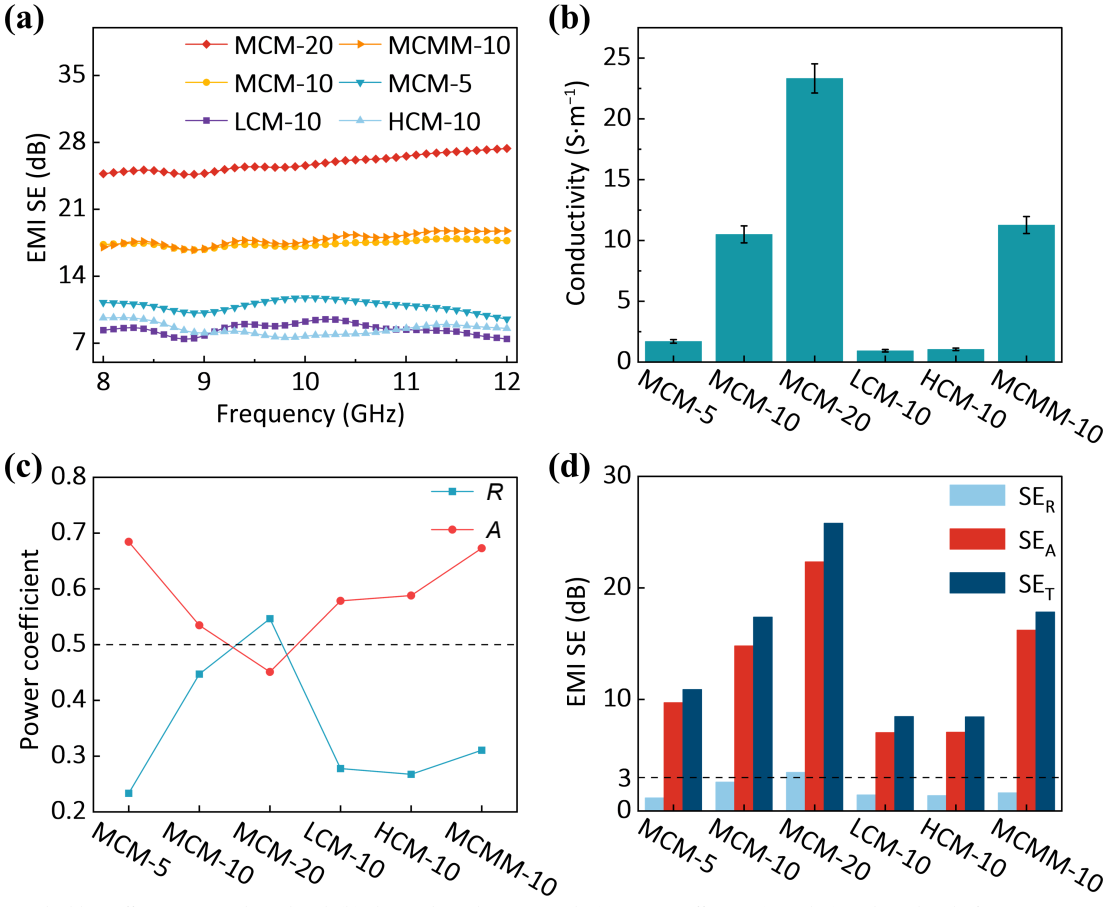

Figure 4 (a) EMI shielding effectiveness in the X-band, (b) electrical conductivity, and (c) power coefficients (*R* and *A*) in the X-band of MCM-5, MCM-10, MCM-20, LCM-10, HCM-10, and MCMM-10. (d) SE_T, SE_A, and SE_R for these aerogels.

adjust its impedance matching. Compared to MCM-10, the composite MCMM-10 exhibited an increase in absorption coefficient by 0.14 while maintaining electrical conductivity within the same order of magnitude. Furthermore, the total shielding effectiveness in the 10–12 GHz frequency band was further enhanced. This reveals that after entering the material, electromagnetic waves are efficiently converted into thermal energy through the synergistic action of multiple reflections and dielectric loss. A comprehensive comparison of the SE_T, absorption shielding effectiveness (SE_A), and reflection shielding effectiveness (SE_R) values for the various samples (Fig. 4(d)) indicates that, except for the high-concentration component MCM-20 which exhibited stronger reflection characteristics, all other systems were dominated by absorption loss. This confirms that this series of aerogels possesses excellent absorption-dominated green shielding properties.

Figures 5(a)–5(c) present the frequency-dependent characteristics of the complex permittivity and dielectric loss tangent (tanδ) for the samples across the X-band (8–12 GHz). The experimental results reveal that both the ε' and ε'' of the complex permittivity for LCM-10 and HCM-10 remain at relatively low levels, indicating a limited capacity for electromagnetic energy storage and dissipation. In contrast, the MCM series exhibits a significant enhancement in dielectric response. Notably, MCM-20 demonstrates the highest ε' and ε'' values, which is attributed to the pronounced charge migration and conductive loss characteristics resulting from the dense network formed by its high MXene loading.

To gain deeper insight into the dielectric relaxation behavior, the Cole–Cole model (Figs. 5(d)–5(i)) was employed to analyze the loss mechanisms. The arc segments for LCM-10 (Fig. 5(d)) and HCM-10 (Fig. 5(e)) are sparse and poorly defined, indicating weak internal dipole relaxation processes. In comparison, MCM-5 (Fig. 5(f)) and MCM-10 (Fig. 5(g)) exhibit multiple Debye relaxation quasi-semicircles, confirming the dominant roles of interfacial polarization (Maxwell–Wagner–Sillars effect) and dipole polarization in energy attenuation. Upon incorporating 1T-MoS_2, the relaxation arcs for MCMM-10 (Fig. 5(h)) become denser and more convergent. This suggests that the introduction of the metallic 1T-phase induces abundant heterogeneous interfaces, strengthening the synergistic effect between polarization loss and conductive loss. It is worth noting that MCM-20 (Fig. 5(i)) displays only a single, large-radius arc. This indicates that, driven by its high conductivity, the dominant loss mechanism has shifted from polarization relaxation to conductive loss [53, 54].

However, superior dielectric loss capability is not the sole determinant of high absorption shielding effectiveness [55–57]. This must be comprehensively explained in conjunction with impedance matching principles and the power coefficients presented in Fig. 4. Although MCM-20 possesses the strongest potential for dielectric loss, its excessively high real permittivity causes the material's characteristic impedance to deviate significantly from the impedance of free space, resulting in intense interface reflection. This phenomenon is corroborated in Figs. 4(c)

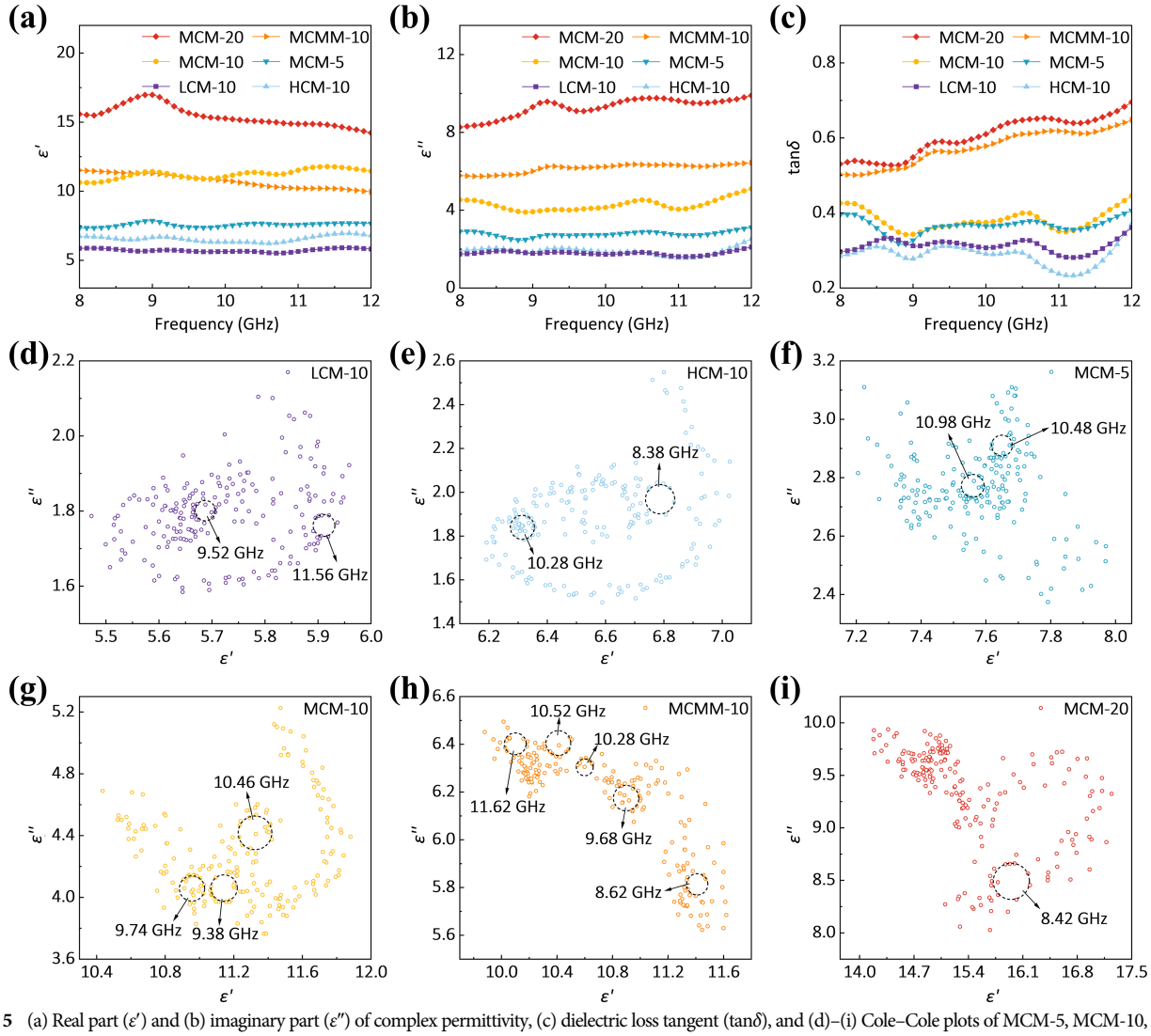

Figure 5 (a) Real part (ε′) and (b) imaginary part (ε″) of complex permittivity, (c) dielectric loss tangent (tanδ), and (d)–(i) Cole–Cole plots of MCM-5, MCM-10, MCM-20, LCM-10, HCM-10, and MCMM-10.

and 4(d), where MCM-20 exhibits the highest reflection shielding and the lowest absorption coefficient. In contrast, MCM-10 and MCMM-10 achieve a balanced window between loss capability and impedance matching by maintaining a moderate dielectric level. This ensures that incident electromagnetic waves can maximally couple into the aerogel's interior and be converted into thermal energy through multiple polarization mechanisms, thereby demonstrating the green shielding characteristic dominated by absorption loss.

3.4 Radar cross-section (RCS) simulation verification

RCS is a key far-field physical parameter for evaluating the electromagnetic wave absorption performance of materials. Its value directly represents the scattering of the incident electromagnetic waves from the material. A lower RCS value indicates that the material can more effectively convert incident wave energy into internal dissipation rather than backscattering it back into space [58, 59]. In this work, CST Microwave Studio (CST-MWS) software was employed to simulate the RCS of the MCM-series aerogel samples, aiming to validate their practical wave-absorption potential in engineering applications from a far-field response perspective. As illustrated in Fig. S6(a) in the ESM, a schematic diagram represents the CST simulation model with dimensions of 150 mm × 150 mm × 6 mm at a frequency of 12 GHz. Figures 6(a)–6(d) present the simulated 3D RCS patterns of the MCM-series aerogel samples. Compared to MCM-5, MCM-10, MCM-20, and PEC (Fig. S6(b) in the ESM), MCMM-10 exhibits significantly lower scattered signal intensity. This demonstrates that constructing the MXene@1T-MoS_2 heterostructure can effectively enhance the material's capability to absorb and dissipate electromagnetic waves. Figures 6(a')–6(d') further display the RCS curves of each sample across the full angular range from −180° to 180°. Among all tested samples, MCMM-10 consistently shows the lowest scattered signal throughout the entire detection angle range, with its RCS values generally below −20 dB·m^2, significantly outperforming other comparative samples and the PEC benchmark.

The results in Fig. 6(e) further confirm that MCMM-10 maintains the lowest RCS level across the full angular range in the *Y*–O–*Z* plane. This excellent far-field absorption performance can be attributed to the synergistic effect of its optimized dielectric loss characteristics and impedance matching properties. Combined with the analysis from Figs. 4 and 5, it is evident that although MCM-20 possesses higher conductivity and permittivity, severe impedance

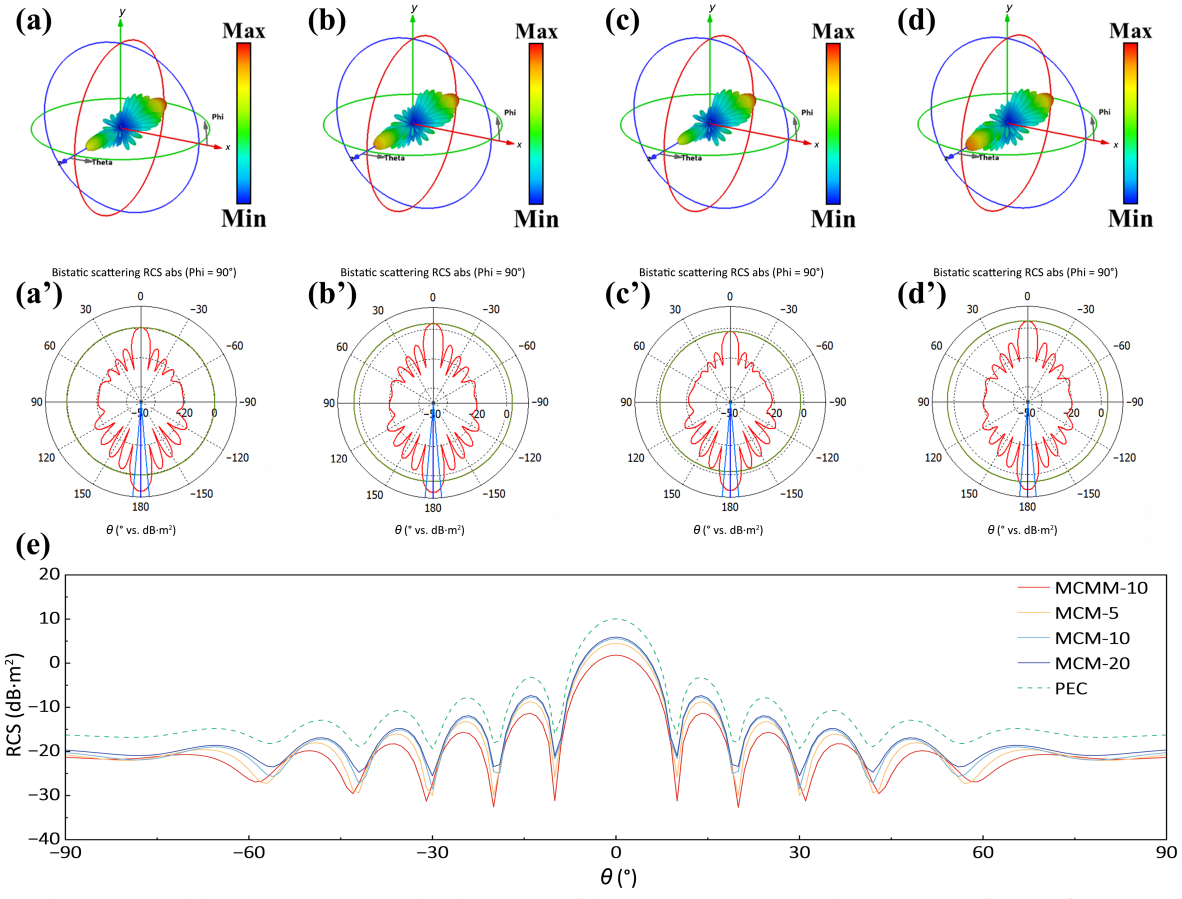

Figure 6 (a)–(d) RCS patterns of the MCM-series aerogels. (a')–(d') RCS values of the MCM-series aerogels over the angular range of $-180° < \theta < 180°$. (e) RCS curves of the perfect electric conductor (PEC) and the MCM-series aerogels under the condition of vertical incidence angle.

mismatch leads to high surface reflection, limiting its far-field absorption performance. In contrast, MCMM-10 utilizes the highly conductive skeleton constructed by MXene to provide conductive loss pathways, while the abundant heterogeneous interfaces formed with 1T-MoS_2 induce strong interfacial polarization and dipole relaxation. This multi-scale, multi-mechanism synergistic loss enables the material to optimize impedance matching while maintaining a moderate permittivity. Incident electromagnetic waves can thus maximally penetrate the aerogel interior and be efficiently dissipated via multiple loss mechanisms within the porous structure, resulting in outstanding absorption performance at the far-field scale.

4 Conclusion

In summary, MXene@1T-MoS_2/chitosan composite aerogels with highly ordered lamellar architectures were successfully fabricated via a chitosan-assisted self-assembly strategy, combined with directional freezing and lyophilization. We found that medium-viscosity chitosan is pivotal in inducing the optimal lamellar porous structure, which constructs a robust 3D conductive network significantly superior to low or high-viscosity systems. By engineering 1T-MoS_2 heterogeneous interfaces, the impedance matching was effectively optimized, shifting the dominant shielding mechanism from reflection to high-efficiency absorption with a 0.14 increase in the absorption coefficient. Far-field simulations further confirmed this superior performance, with RCS values consistently suppressed below -20 dB·m² across a wide angular range. This outstanding green shielding stems from the synergistic integration of conductive loss, interfacial polarization triggered by the Maxwell–Wagner–Sillars effect, and multiple internal reflections. This work offers profound insights into the structural regulation of 2D nanomaterials for developing lightweight, absorption-dominated electromagnetic protection materials.

Electronic Supplementary Material: Supplementary material (photograph of the composite chitosan aerogel, XPS, elemental mapping, schematic diagram of the waveguide method, and RCS pattern of the PEC) is available in the online version of this article at https://doi.org/10.26599/NR.2026.94908766 .

Data availability

All data needed to support the conclusions in the paper are presented in the manuscript and the Electronic Supplementary Material. Additional data related to this paper may be requested from the corresponding author upon request.

Acknowledgements

The authors gratefully acknowledge the project supported by the National Natural Science Foundation Joint Fund for Regional Innovation and Development (No. U24A20299) and Postgraduate Research & Practice Innovation Program of Jiangsu Province (No. SJCX25_0323).

Declaration of competing interest

All the contributing authors report no conflict of interests in this work.

Author contribution statement

S. J. S.: Data curation, project administration, conceptualization, validation, writing – original draft, experimental design. S. J. L.: Data curation, formal analysis, writing – review & editing, visualization. Z. Y. S.: Writing – review & editing, visualization. Z. F.: Writing – review & editing. W. K. F.: Validation. X. H.: Validation. W. P. Z.: Investigation, software, formal analysis. B. L.: Resources, supervision, methodology. L. L. W.: Resources, funding acquisition, supervision, project administration.

Use of AI statement

None.

References

[1] Halder, K. K.; Tomar, M.; Sachdev, V. K.; Gupta, V. Carbonized charcoal-loaded PVDF polymer composite: A promising EMI shielding material. *Arab. J. Sci. Eng.* **2020**, *45*, 465–474.

[2] Wei, H. Y.; Zhang, Z. P.; Hussain, G.; Zhou, L. S.; Li, Q.; Ostrikov, K. Techniques to enhance magnetic permeability in microwave absorbing materials. *Appl. Mater. Today* **2020**, *19*, 100596.

[3] Sun, Z. P.; Chen, J. L.; Jia, X. C.; Wang, G. Q.; Shen, B.; Zheng, W. G. Humidification of high-performance and multifunctional polyimide/carbon nanotube composite foams for enhanced electromagnetic shielding. *Mater. Today Phys.* **2021**, *21*, 100521.

[4] Khan, S. U. D.; Arora, M.; Wahab, M. A.; Saini, P. Permittivity and electromagnetic interference shielding investigations of activated charcoal loaded acrylic coating compositions. *J. Polym.* **2014**, *2014*, 193058.

[5] Wang, X. Y.; Liao, S. Y.; Wan, Y. J.; Zhu, P. L.; Hu, Y. G.; Zhao, T.; Sun, R.; Wong, C. P. Electromagnetic interference shielding materials: Recent progress, structure design, and future perspective. *J. Mater. Chem. C* **2022**, *10*, 44–72.

[6] Rong, Y. J.; Guo, H. T.; Zhou, X.; Wu, W. J.; Zhu, W. K.; Wang, H. W.; Ma, X. F.; Jiang, S. H.; Sun, Q. F. Absorption-dominant electromagnetic interference shielding materials: From microstructure to multi-scale assembly. *Adv. Funct. Mater.* **2025**, *35*, e06746.

[7] Gao, S.; Xu, J. C.; Cao, J. Q.; Yao, H. M.; Ali, S. E.; Abo-Dief, H. M.; Alanazi, A. K.; Lan, C. W.; Algadi, H.; Zhai, X. J. Highly efficient tunable terahertz all-dielectric metasurface absorber based on high mode. *Adv. Compos. Hybrid Mater.* **2023**, *6*, 116.

[8] Kumar, P. Ultrathin 2D nanomaterials for electromagnetic interference shielding. *Adv. Mater. Interfaces* **2019**, *6*, 1901454.

[9] Chung, D. D. L. Electromagnetic interference shielding effectiveness of carbon materials. *Carbon* **2001**, *39*, 279–285.

[10] Tong, H.; Zhu, G.; Mao, W. Development of EMI shielding materials characterized by low secondary electromagnetic radiation pollution. In *2011 Second International Conference on Mechanic Automation and Control Engineering*, Inner Mongolia, China, 2011, pp 2075–2077.

[11] Song, Y.; Yin, F. X.; Zhang, C. W.; Guo, W. B.; Han, L. Y.; Yuan, Y. Three-dimensional ordered mesoporous carbon spheres modified with ultrafine zinc oxide nanoparticles for enhanced microwave absorption properties. *Nano-Micro Lett.* **2021**, *13*, 76.

[12] Xiong, C. Y.; Zheng, C. M.; Zhang, Z.; Xiong, Q.; Zhou, Q. S.; Li, D. P.; Shen, M. X.; Ni, Y. H. Polyaniline@cellulose nanofibers multifunctional composite material for supercapacitors, electromagnetic interference shielding and sensing. *J. Materiomics* **2025**, *11*, 100841.

[13] Lim, K. R. G.; Shekhirev, M.; Wyatt, B. C.; Anasori, B.; Gogotsi, Y.; Seh, Z. W. Fundamentals of MXene synthesis. *Nat. Synth.* **2022**, *1*, 601–614.

[14] Li, M. K.; Sun, Y. Y.; Feng, D. Y.; Ruan, K. P.; Liu, X.; Gu, J. W. Thermally conductive polyvinyl alcohol composite films via introducing hetero-structured MXene@silver fillers. *Nano Res.* **2023**, *16*, 7820–7828.

[15] Li, X. J.; Shen, M. X.; Sun, J. J.; Xiong, C. Y.; Liu, Y. J.; Hou, L.; Hua, F. G. Bottom-up assembly of biomass-derived MXene aerogels with hierarchical electromagnetic interfaces for multifunctional electromagnetic wave absorption. *Small* **2026**, *22*, e10286.

[16] Han, M. K.; Shuck, C. E.; Rakhmanov, R.; Parchment, D.; Anasori, B.; Koo, C. M.; Friedman, G.; Gogotsi, Y. Beyond $Ti_3C_2T_x$: MXenes for electromagnetic interference shielding. *ACS Nano* **2020**, *14*, 5008–5016.

[17] Cao, W.; Nie, J. L.; Cao, Y.; Gao, C. J.; Wang, M. S.; Wang, W. W.; Lu, X. L.; Ma, X. H.; Zhong, P. A review of how to improve $Ti_3C_2T_x$ MXene stability. *Chem. Eng. J.* **2024**, *496*, 154097.

[18] Ye, Z. H.; Zhao, D. Q.; Liu, F. H.; Luo, J. J.; Liu, X. L.; Zhao, W. W. Flexible and highly conductive $Ti_3C_2T_x$/natural rubber composites with interconnected networks for high-performance electromagnetic interference shielding. *Compos. Part A: Appl. Sci. Manuf.* **2024**, *180*, 108067.

[19] Zhao, S.; Zhang, H. B.; Luo, J. Q.; Wang, Q. W.; Xu, B.; Hong, S.; Yu, Z. Z. Highly electrically conductive three-dimensional $Ti_3C_2T_X$ MXene/reduced graphene oxide hybrid aerogels with excellent electromagnetic interference shielding performances. *ACS Nano* **2018**, *12*, 11193–11202.

[20] Jiang, X. W.; Wang, Q.; Song, L. M.; Lu, H. X.; Xu, H. L.; Shao, G.; Wang, H. L.; Zhang, R.; Wang, C. G.; Fan, B. B. Enhancing electromagnetic wave absorption with core–shell structured SiO_2@MXene@MoS_2 nanospheres. *Carbon Energy* **2024**, *6*, e502.

[21] Liu, Y. J.; Zhou, J. T.; Li, C. C.; Zhang, H. H.; Wang, Y. C.; Yan, Y.; Duan, L.; Cheng, Z. Y.; Ma, Y.; Yao, Z. J. Interfacial coupling effects in two-dimensional ordered arrays for microwave attenuation. *Nat. Commun.* **2025**, *16*, 202.

[22] Askari, M. B.; Salarizadeh, P. Molybdenum disulfide (MoS_2) as a promising transition metal chalcogenide for supercapacitor electrodes: A comprehensive review. *Mater. Renew. Sustain. Energy* **2025**, *14*, 55.

[23] Cheng, J. B.; Zhao, H. B.; Cao, M.; Li, M. E.; Zhang, A. N.; Li, S. L.; Wang, Y. Z. Banana leaflike C-doped MoS_2 aerogels toward excellent microwave absorption performance. *ACS Appl. Mater. Interfaces* **2020**, *12*, 26301–26312.

[24] Yu, Y. F.; Nam, G. H.; He, Q. Y.; Wu, X. J.; Zhang, K.; Yang, Z. Z.; Chen, J. Z.; Ma, Q. L.; Zhao, M. T.; Liu, Z. Q. et al. High phase-purity 1T'-MoS_2-and 1T'-$MoSe_2$-layered crystals. *Nat. Chem.* **2018**, *10*, 638–643.

[25] Cheng, Y.; Li, X. Y.; Qin, Y. X.; Fang, Y. T.; Liu, G. L.; Wang, Z. Y.; Matz, J.; Dong, P.; Shen, J. F.; Ye, M. X. Hierarchically porous polyimide/$Ti_3C_2T_x$ film with stable electromagnetic interference shielding after resisting harsh conditions. *Sci. Adv.* **2021**, *7*, eabj1663.

[26] Chen, L. F.; Ong, C. K.; Neo, C. P.; Varadan, V. V.; Varadan, V. K. *Microwave Electronics: Measurement and Materials Characterization*; Wiley: Chichester, 2004.

[27] Wang, S. B.; Liu, Y.; Liu, Y. Y.; Hu, W. B. Effect of HF etching on titanium carbide ($Ti_3C_2T_x$) microstructure and its capacitive properties. *Chem. Eng. J.* **2023**, *452*, 139512.

[28] Yang, Z. J.; Li, Z. N.; Lampronti, G. I.; Lee, J. I.; Wang, Y.; Day, J.; Chhowalla, M. Environmental and thermal stability of chemically exfoliated Li_xMoS_2 for lithium-sulfur batteries. *Chem. Mater.* **2024**, *36*, 4829–4837.

[29] Yuan, Z. H.; Zhou, B. L.; Yuan, K. Y.; Xie, Z. J.; Zheng, K.; Wang, H. Q.; Jiao, C. L.; Ye, D. D. High-aligned oppositely-charged nanocellulose/MXene aerogel membranes through synergy of directional freeze-casting and structural densification for osmotic-energy harvesting. *Nano Energy* **2024**, *124*, 109450.

[30] Liang, W. H.; Wu, J. T.; Zhang, S.; Zhao, P. Y.; Cong, Y.; Guo, Y. Q.;

Wang, G. S. Porous $Ti_3C_2T_x$ MXene nanosheets sandwiched between polyimide fiber mats for electromagnetic interference shielding. *Nano Res.* **2024**, *17*, 2070–2078.
[31] Liu, J.; Zhang, H. B.; Sun, R. H.; Liu, Y. F.; Liu, Z. S.; Zhou, A. G.; Yu, Z. Z. Hydrophobic, flexible, and lightweight MXene foams for high-performance electromagnetic-interference shielding. *Adv. Mater.* **2017**, *29*, 1702367.
[32] Liang, C. B.; Qiu, H.; Song, P.; Shi, X. T.; Kong, J.; Gu, J. W. Ultra-light MXene aerogel/wood-derived porous carbon composites with wall-like "mortar/brick" structures for electromagnetic interference shielding. *Sci. Bull.* **2020**, *65*, 616–622.
[33] Zhang, Y. L.; Ma, Z. L.; Ruan, K. P.; Gu, J. W. Multifunctional $Ti_3C_2T_x$-(Fe_3O_4/polyimide) composite films with Janus structure for outstanding electromagnetic interference shielding and superior visual thermal management. *Nano Res.* **2022**, *15*, 5601–5609.
[34] Chen, Y. T.; Liu, L. X.; Cai, L. J.; Mu, G. Q.; Ju, T.; Wei, M.; Li, Z. H.; Lu, Z. T.; Wang, N.; Zhang, T. P. et al. High-performance wet adhesion of wood with chitosan. *ACS Sustain. Chem. Eng.* **2024**, *12*, 4946–4956.
[35] He, X.; Xu, Y. Z.; Wang, Y.; Wu, L. H.; Chen, F. F.; Yu, Y. Synergistic effect of GO and MXene enables ultrasensitive, reversible, and self-powered fire warning of a GO/MXene/chitosan aerogel. *ACS Appl. Mater. Interfaces* **2024**, *16*, 59346–59357.
[36] Le, D. T.; Carbonnier, B.; Hamadi, S.; Grande, D.; Fois, M.; Naili, S.; Nguyen, V. H.; Mahouche-Chergui, S. Toward the development of graphene/chitosan biocomposite aerogels with enhanced mechanical and thermal insulation performance. *ACS Appl. Polym. Mater.* **2024**, *6*, 13132–13146.
[37] Takeshita, S.; Zhao, S. Y.; Malfait, W. J.; Koebel, M. M. Chemistry of chitosan aerogels: Three-dimensional pore control for tailored applications. *Angew. Chem., Int. Ed.* **2021**, *60*, 9828–9851.
[38] Chen, K. X.; Liu, M.; Shi, Y. Q.; Wang, H. R.; Fu, L. B.; Feng, Y. Z.; Song, P. G. Multi-hierarchical flexible composites towards superior fire safety and electromagnetic interference shielding. *Nano Res.* **2022**, *15*, 9531–9543.
[39] Xue, T. T.; Yang, Y.; Yu, D. Y.; Wali, Q.; Wang, Z. Y.; Cao, X. S.; Fan, W.; Liu, T. X. 3D printed integrated gradient-conductive MXene/CNT/polyimide aerogel frames for electromagnetic interference shielding with ultra-low reflection. *Nano-Micro Lett.* **2023**, *15*, 45.
[40] Li, Z. K.; Hu, J.; Guan, W. W.; Xiong, X. Q.; Long, H. Z.; Wang, X. Z. Three-dimensional macroporous reduced graphene oxide-mxene aerogel decorated with hollow mesoporous carbon spheres for absorption-dominant electromagnetic interference shielding and efficient oil/water separation. *ACS Sustain. Chem. Eng.* **2024**, *12*, 12683–12694.
[41] Yang, G. Y.; Yao, X. M.; Li, Y. J.; Hu, Y.; Chen, X.; Li, J. L.; Chen, J. Z.; Jiang, J. J. $Ti_3C_2T_x$ MXene nanosheet-based hybrid films for enhanced wave absorption-dominated electromagnetic interference shielding. *ACS Appl. Nano Mater.* **2023**, *6*, 19378–19391.
[42] Dhugga, L. K.; Baskey, H. B.; Gaur, K. K.; Singh, D. P. Multiple interfacial polarization relaxation induced amelioration in microwave dielectric and EMI shielding of polypyrrole based nanocomposites. *Compos. Struct.* **2026**, *376*, 119844.
[43] Liu, J. L.; Liang, H. S.; Wu, H. J. Hierarchical flower-like Fe_3O_4/MoS_2 composites for selective broadband electromagnetic wave absorption performance. *Compos. Part A: Appl. Sci. Manuf.* **2020**, *130*, 105760.
[44] Zhao, B.; Ma, Z. L.; Sun, Y. Y.; Han, Y. X.; Gu, J. W. Flexible and robust $Ti_3C_2T_x$/(ANF@FeNi) composite films with outstanding electromagnetic interference shielding and electrothermal conversion performances. *Small Struct.* **2022**, *3*, 2200162.
[45] Wang, J. E.; Ming, W.; Chen, L. F.; Song, T. L.; Yele, M.; Zhang, H.; Yang, L.; Sarula, G.; Liang, B. L.; Yan, L. T. et al. MoS_2 lubricate-toughened MXene/ANF composites for multifunctional electromagnetic interference shielding. *Nano-Micro Lett.* **2025**, *17*, 36.
[46] Jia, Z. R.; Liu, J. K.; Gao, Z. G.; Zhang, C. H.; Wu, G. L. Molecular intercalation-induced two-phase evolution engineering of 1T and 2H-MS_2 (M = Mo, V, W) for interface-polarization-enhanced electromagnetic absorbers. *Adv. Funct. Mater.* **2025**, *35*, 2405523.
[47] Cheng, Y.; Zhu, W. D.; Lu, X. F.; Wang, C. One-dimensional metallic, magnetic, and dielectric nanomaterials-based composites for electromagnetic wave interference shielding. *Nano Res.* **2022**, *15*, 9595–9613.
[48] Sima, H. F.; Liu, B.; Shi, X. L.; Zhang, C. L. CNT@CNF/MXene hydrogel with complete conductive network for flexible anti-freeze sensor and electromagnetic shielding. *Carbohydr. Polym.* **2025**, *366*, 123825.
[49] Wang, T. X.; Xiong, C. Y.; Li, P. Y. Manufacturing strategies for cellulose-based EMI shielding composites: Process-driven microstructures and EMI shielding performance. *Compos. Part B: Eng.* **2026**, *309*, 113093.
[50] Ding, B. H.; Wang, Y. X.; Li, Y. F.; Jiang, H. T.; Gao, P. Y.; Sun, Y.; Guo, J. H.; Teng, C. Lightweight, rigid, ordered RSF/PVA/MXene aerogels with Janus structure for effective electromagnetic interference shielding with low reflectivity. *Nano Res.* **2026**, *19*, 94908069.
[51] Han, C.; Zheng, Q.; Xiang, K.; Zhang, M.; Cao, M. S. Self-assembly of one-dimensional cobalt-carbon to turn dielectric properties for electromagnetic attenuation. *Carbon* **2025**, *236*, 120103.
[52] Yao, H. M.; Yang, J. P.; Li, H.; Xu, J. C.; Bi, K. Optimal design of multilayer radar absorbing materials: A simulation-optimization approach. *Adv. Compos. Hybrid Mater.* **2023**, *6*, 43.
[53] Hu, X. F.; Zhang, Y. L.; Guo, H.; He, M. K.; Qiu, H.; Shi, X. T.; Wang, L.; Gu, J. W. Multifunctional flexible WPU composite aerogels with sandwich structure for dual-sided low-reflection electromagnetic interference shielding. *Adv. Funct. Mater.* **2026**, *36*, e17665.
[54] Zhang, S. J.; Pei, Y. X.; Zhao, Z. W.; Guan, C. L.; Wu, G. L. Simultaneous manipulation of polarization relaxation and conductivity toward self-repairing reduced graphene oxide based ternary hybrids for efficient electromagnetic wave absorption. *J. Colloid Interface Sci.* **2023**, *630*, 453–464.
[55] Cheng, J. Y.; Jin, Y. H.; Zhao, J. H.; Jing, Q.; Gu, B. L.; Wei, J. L.; Yi, S. H.; Li, M. M.; Nie, W. L.; Qin, Q. H. et al. From VIB-to VB-group transition metal disulfides: Structure engineering modulation for superior electromagnetic wave absorption. *Nano-Micro Lett.* **2024**, *16*, 29.
[56] Wu, M.; Wang, H. C.; Liang, X. H.; Wang, D. H. Efficient and tunable microwave absorbers of the flower-like 1T/2H–MoS_2 with hollow nanostructures. *J. Alloys Compd.* **2023**, *933*, 167763.
[57] Wu, Y. F.; Li, Q. S.; Li, Y. Z.; Li, C.; Zhou, Y. Q.; Du, P.; Cao, W. T.; He, X.; Liu, Z. A.; Xu, J. C. et al. Roll-to-roll joule-heating to construct ferromagnetic carbon fiber felt for superior electromagnetic interference shielding. *Carbon* **2024**, *229*, 119474.
[58] Chen, Y. Z.; Gai, L. X.; Hu, B.; Wang, Y.; Chen, Y. Y.; Han, X. J.; Xu, P.; Du, Y. C. Directional three-dimensional macroporous carbon foams decorated with WC_{1-x} nanoparticles derived from salting-out protein assemblies for highly effective electromagnetic absorption. *Nano-Micro Lett.* **2026**, *18*, 71.
[59] Wang, S. N.; Cheng, Z. Y.; Yan, Y.; Yao, J. R.; Liu, Y. J.; Tao, J. Q.; Duan, L.; Weng, Y. L.; Zhu, H. B.; Zhuang, H. Y. et al. Programmable electromagnetic switching in shape-memory-driven liquid metal/polyimide/aramid nanofiber aerogels for intelligent wave management. *Adv. Funct. Mater.* **2026**, *36*, e21612.